The current issue and full text archive of this journal is available at
www.emeraldinsight.com/0961-5539.htm

Received 4 July 2006
Revised 8 March 2007
Accepted 28 March 2007

Turbulent flow and heat transfer in stationary and rotating cooling passages with inclined ribs on opposite walls

Hector Iacovides
School of Mechanical, Aerospace and Civil Engineering, University of Manchester, Manchester, UK, and
Mehrdad Raisee
Department of Mechanical Engineering, Faculty of Engineering, University of Tehran, Tehran, Iran

Abstract

Purpose – This paper aims to compute flow and heat transfer through a straight, orthogonally rotating duct, with ribs along the leading and trailing walls, in a staggered arrangement and at an angle of 45° to the main flow direction.

Design/methodology/approach – Flow computations have been produced using a 3D non-orthogonal flow solver, with two two-layer models of turbulence (an effective-viscosity model and a second-moment closure), in which across the near-wall regions the dissipation rate of turbulence is obtained from the wall distance. Flow comparisons have been carried out for a Reynolds number of 100,000 and for rotation numbers of 0 (stationary) and 0.1. Temperature comparisons have been obtained for a Reynolds number of 36,000, a Prandtl number of 5.9 (water) and rotation numbers of 0 and 0.2 and also at a Prandtl number of 0.7 (air) and a rotation number of 0.

Findings – It was found that both two-layer models returned similar flow and thermal predictions which are also in close agreement with the flow and thermal measurements. The flow and thermal developments are found to be dominated by the rib-induced secondary motion, which leads to strong span-wise variations in the mean flow and the local Nusselt number and to a uniform distribution of turbulence intensities across the duct. Rotation causes the development of stronger secondary motion along the pressure side of the duct and also the transfer of the faster fluid to this side. The thermal predictions, especially those of the second-moment closure, reproduce the levels and most of the local features of the measured Nusselt number, but over the second half of the rib interval over-predict the local Nusselt number.

Originality/value – The work contributes to the understanding of the flow and thermal development in cooling passages of gas turbine blades, and to the validation of turbulence models that can be used for their prediction, at both effective viscosity and second-moment closure levels.

Keywords Turbines, Cooling, Turbulent flow, Modelling, Gas flow

Paper type Research paper

International Journal of Numerical Methods for Heat & Fluid Flow
Vol. 18 No. 2, 2008
pp. 258-278

0961-5539
DOI 10.1108/09615530810846374

The research reported here is sponsored by the UK Science and Engineering Research Council, under Grant No GR/R03433. Authors' names are listed alphabetically.

1. Introduction

Heat-transfer-enhancing ribs are now routinely employed in blade cooling applications. They are usually employed along two opposite surfaces of internal passages within rotating blades. Moreover, the trend in recent years has been to align these ribs at an angle to the main flow direction. There is consequently a need to improve our understanding of the flow and thermal development in such passages and also to establish how reliably they can be numerically predicted. Investigations of heat transfer through passages with inclined ribs have already appeared in the scientific literature. Taslim *et al.* (1996), Han *et al.* (1988), Han and Zhang (1991) and Johnson *et al.* (1994) present experimental data for either heat or mass transfer and the friction factor, which aim to show the effects of rib orientation, the Coriolis force and rotational buoyancy on the axial variation of the Nusselt number average on each duct side. Experimental studies that provide detailed flow measurements for ducts with inclined ribs have also emerged more recently (Bonhoff *et al.*, 1999; Liou and Dai, 2003). One of the findings of Liou and Dai (2003) is that for the experimental model used, orthogonal rotation prevented the establishment of periodic conditions, even after about seven rib intervals. Experimental studies that produce both local flow and thermal data for rotating passages with inclined ribs are still rare. Numerical studies that show computations of heat and fluid flow through ducts with inclined ribs have also started to appear. Bonhoff *et al.* (1997), Jang *et al.* (2001), Lin *et al.* (2001) and Al-Qahtani *et al.* (2002a, b) have looked at either straight ducts with inclined ribs, or *U*-bends with ribbed upstream and downstream sections. They have produced computations that reveal many of the complex flow features that develop. Moreover, these numerical studies also show how the wall heat transfer is influenced by rib orientation, the Coriolis force and rotational buoyancy, the duct aspect ratio and the orientation of the duct relative to the axis of rotation. These studies certainly contribute a lot to our understanding of the flow physics and their effects on the thermal behavior, but, due to the lack of sufficiently detailed experimental data for the cases computed, include comparisons with only spot values of the side-averaged Nusselt number. The only exception is Bonhoff *et al.* (1999) in which extensive local flow comparisons are presented for stationary conditions. There is clearly a need for validation studies that present more extensive comparisons between measured and computed local flow and heat transfer data.

The authors' research group has been engaged in the experimental and computational investigation of blade cooling flows for over a decade (Iacovides and Launder, 1995; Iacovides *et al.*, 1998, 2000; Iacovides, 1998; Iacovides and Raisee, 1999). A particular feature of our experimental investigations has been the fact that we have been able to produce both local thermal and hydrodynamic data for internal cooling flows. The outcome of our investigations of cooling flows through passages with normal ribs has already been documented (Iacovides and Launder, 1995; Iacovides *et al.*, 1998, 2000; Iacovides, 1998; Iacovides and Raisee, 1999). It was shown that the flow development was well predicted by all the turbulence models employed, while the wall heat transfer was more reliably predicted by low-Reynolds-number models, especially at the second-moment-closure level. In contrast to our numerical simulations of flows through cooling passages with ribs normal to the flow direction, a more recent study focusing on stationary cooling passages with inclined 45°-ribs (Iacovides *et al.*, 2003) showed that under such conditions, more economical, two-layer, approaches can

also produce satisfactory heat and fluid flow computations, especially when used with second-moment closures. In two-layer approaches, as the name implies, within the near-wall regions the dissipation rate of turbulence is obtained from an algebraic equation in terms of the wall distance. This is the reason for the improved numerical robustness of these approaches to the modeling of near-wall turbulence, in comparison to low-Reynolds number models. The latter require finer near-wall grids.

Here, we present the results of a more comprehensive numerical study of heat and fluid flow through cooling passages with ribs inclined at a 45°-angle to the flow direction. In addition to the computations we presented in Iacovides *et al.* (2003) for heated flow in a stationary passage with water as the working fluid ($Pr = 5.9$), here we also add heat transfer computations for air ($Pr = 0.71$), under stationary conditions, while the water flow hydrodynamic and thermal comparisons are now extended to rotating conditions. Comparisons with local flow (LDA) and also local thermal (liquid crystal) measurements, presented in Iacovides *et al.* (2003, 2001) and Garcia (1998), allow for a more thorough assessment of the suitability of two-layer models for the computation of cooling flows in rotating passages with inclined ribs. Moreover, comparisons between flow predictions in stationary and rotating passages help explain how rotation affects the flow development in passages with inclined ribs and how the resulting flow structures influence the thermal characteristics.

2. The numerical solver

2.1 Mean flow equations

All the equations are presented in Cartesian tensor notation, for a rotating frame of reference. For a steady incompressible flow, the conservation laws of mass, momentum and energy are written as:

- *Continuity:*

$$\frac{\partial(\rho U_j)}{\partial x_j} = 0 \tag{1}$$

- *Momentum:*

$$\frac{\partial(\rho U_j U_i)}{\partial x_j} = -\frac{\partial P}{\partial x_i} + \frac{\partial}{\partial x_j}\left[\mu\left(\frac{\partial U_i}{\partial x_j} + \frac{\partial U_j}{\partial x_i}\right) - \overline{u_i u_j}\right] - 2\rho\varepsilon_{ijp}\mathbf{\Omega}_p U_j - \rho[\Omega_j \mathbf{X}_j \mathbf{\Omega}_i - \mathbf{\Omega}_j \mathbf{X}_i \mathbf{\Omega}_j] \tag{2}$$

- *Energy:*

$$\frac{\partial(\rho U_j T)}{\partial x_j} = \frac{\partial}{\partial x_j}\left(\frac{\mu}{\mathrm{Pr}}\frac{\partial T}{\partial x_j} - \rho\overline{u_j t}\right) \tag{3}$$

In equation (2) above, $\mathbf{\Omega}_p$ denotes the rotation vector of the coordinate system and $\mathbf{X}_i$ the position vector. The first group of rotation terms in equation (2) represent the Coriolis forces and the second group the centrifugal forces. The fluid density here is assumed to remain constant, because the experimental data used to validate these computations have been obtained for either isothermal conditions (flow data), or, in the case of the thermal data, involve temperature differences small enough for the density

to be practically constant. The centrifugal terms therefore do not influence the flow development.

2.2 Turbulence modeling equations

As mentioned in the introduction, two two-layer models of turbulence have been used, an effective-viscosity model and a differential stress model (DSM). In the effective-viscosity model, the standard $k - \varepsilon$ model, employed in most of the flow domain, is matched to Wolfshtein's (1969) 1-equation model across the near-wall regions. This modeling approach allows the resolution of the mean motion across the sub-layer regions, but without the need for very fine grid resolutions associated with low-Reynolds-number models, in which the dissipation rate equation is integrated up to the wall. For the same reason, in the DSM employed, while the transport equations for the turbulence stresses are integrated up to the wall, the near-wall dissipation rate of turbulence is again obtained from the wall distance.

2.2.1 Two-layer k $-$ *ε/1-equation model.* The turbulent stresses and turbulent heat fluxes are obtained from:

$$\overline{u_i u_j} = -\nu_t \left(\frac{\partial U_i}{\partial x_j} + \frac{\partial U_j}{\partial x_i} \right) + \frac{2}{3}\, \delta_{ij} k \tag{4}$$

$$\overline{u_i t} = -\frac{\nu_t}{\sigma_T}\, \frac{\partial T}{\partial x_i} \tag{5}$$

The high-*Re* $k - \varepsilon$ in the fully turbulent core consists of the following equations:

$$\frac{\partial}{\partial x_j}(\rho U_j k) = \frac{\partial}{\partial x_j} \left[\left(\mu + \frac{\mu_t}{\sigma_k} \right) \frac{\partial k}{\partial x_j} \right] + P_k - \rho\varepsilon \tag{6}$$

$$P_k = -\rho \overline{u_i u_j} \frac{\partial U_i}{\partial x_j} \tag{7}$$

$$\frac{\partial}{\partial x_j}(\rho U_j \varepsilon) = \frac{\partial}{\partial x_j} \left[\left(\mu + \frac{\mu_t}{\sigma_\varepsilon} \right) \frac{\partial \varepsilon}{\partial x_j} \right] + c_{\varepsilon 1} \frac{\varepsilon}{k} P_k - \rho c_{\varepsilon 2} \frac{\varepsilon^2}{k} \tag{8}$$

$$\mu_t = \rho c_\mu \frac{k^2}{\varepsilon} \tag{9}$$

In the 1-equation model, the k-transport equation is the same as equation (6) for the high-*Re* $k - \varepsilon$ while the dissipation rate, ε, and the turbulent viscosity, μ_t, are obtained from:

$$\varepsilon = \frac{k^{3/2}}{\ell_\varepsilon} \tag{10}$$

and:

$$\mu_t = \rho c_\mu \ell_\mu \sqrt{k} \tag{11}$$

The length scales ℓ_ε and ℓ_μ are obtained from the near-wall distance y, according to:

$$\ell_\varepsilon = 2.55y[1 - \exp(-0.236y^*)] \tag{12}$$

$$\ell_\mu = 2.55y[1 - \exp(-0.016y^*)] \tag{13}$$

The dimensionless distance y^* is defined as $yk^{1/2}/\nu$.

2.2.2 Two-layer DSM model. The DSM closure employed here is a rather simple and empirically derived extension to the basic DSM model, that relies on the linear terms for the redistribution of turbulence and uses the wall-reflection terms to reproduce the wall preferential damping of turbulence in the direction normal to it. It has evolved from the low-*Re* algebraic stress closure (ASM) proposed by Iacovides and Launder (1992), which was initially applied to flow and heat transfer through *U*-bends of mild curvature. The low-*Re* ASM closure was subsequently extended by Iacovides and Toumpanakis (1993) to DSM closures which were initially applied to the computation of turbulent flows through rotating cavities. This DSM closure has also been recently applied by Iacovides and Raisee (1999) to the computation of flow and heat transfer through ribbed passages with ribs normal to the flow direction.

Instead of the effective viscosity approximation, equation (4), the turbulent stresses are now obtained through the solution of separate transport equations, represented by equation (14) below:

$$\frac{\partial}{\partial x_k}(\rho U_k \overline{u_i u_j}) = \frac{\partial}{\partial x_k}\left[\left(\mu + \frac{\mu_t}{\sigma_k}\right)\frac{\partial \overline{u_i u_j}}{\partial x_k}\right] + P_{ij} - \rho\varepsilon_{ij} + \phi_{ij} - \left[H_{ij} - \frac{1}{3}H_{kk}\delta_{ij}\right] + J_{ij} \tag{14}$$

As in the k and ε transport equations, the transport of the turbulent stresses due to turbulent mixing is modeled through the effective diffusivity concept. The term P_{ij} denotes the generation rate of the turbulent stresses and is obtained through the exact expression given in equation (15):

$$P_{ij} = -\rho\left(\overline{u_i u_k}\frac{\partial U_j}{\partial x_k} + \overline{u_j u_k}\frac{\partial U_i}{\partial x_k}\right) - 2\rho\Omega_p(\varepsilon_{ipq}\overline{u_q u_j} + \varepsilon_{jpq}\overline{u_q u_i}) \tag{15}$$

$$\varepsilon_{ij} = \frac{2}{3}(1 - f_\varepsilon)\varepsilon\delta_{ij} + f_\varepsilon\frac{\overline{u_i u_j}}{k}\,\varepsilon \tag{16}$$

Note that in contrast to the generation rate term for the turbulent kinetic energy, P_k in equation (7), P_{ij} also includes contributions from the Coriolis force. Because, as noted earlier, the effects of rotational buoyancy are negligible in the cases considered here, further contribution to P_{ij} and to P_k, arising from the centrifugal force, are ignored. The term ε_{ij} denotes the dissipation rate of the turbulent stresses which, as shown in equation (16), is assumed to be isotropic when the flow is fully turbulent and in the near-wall regions becomes proportional to the ratio between the turbulent stress and the turbulent kinetic energy:

$$\phi_{ij} = -c_1\frac{\varepsilon}{k}\left(\overline{u_i u_j} - \frac{2}{3}k\delta_{ij}\right) - c_2\left(P_{ij} - \frac{2}{3}P_k\delta_{ij}\right) + f_w\left(\phi_{ij1}^w + \phi_{ij2}^w\right) \tag{17}$$

The term ϕ_{ij}, given in equation (17), represents the redistribution of turbulent energy among the different components of the Reynolds. Terms ϕ_{ij1}^w and ϕ_{ij2}^w, given in equations (18) and (19), are the conventional wall reflection terms, proposed by Gibson and Launder (1978), to model the "wall-echo" part of the pressure strain correlation, which, near solid surfaces, removes kinetic energy from the fluctuating component

normal to the wall and redistributes in the other two directions. They make use of the wall distance x_n and the unit vector normal to the wall n_i:

$$\phi_{ij1}^{w} = c_1^{w}\frac{\varepsilon}{k}\left(\overline{u_k u_m}n_k n_m \delta_{ij} - \frac{3}{2}\overline{u_k u_i}n_k n_j - \frac{3}{2}\overline{u_k u_j}n_k n_i\right)\left\{\frac{k^{1.5}}{\varepsilon c_l x_n}\right\} \tag{18}$$

$$\phi_{ij2}^{w} = c_2^{w}\frac{\varepsilon}{k}\left(\phi_{km2}n_k n_m \delta_{ij} - \frac{3}{2}\phi_{ik2}n_k n_j - \frac{3}{2}\phi_{jk2}n_k n_i\right)\left\{\frac{k^{1.5}}{\varepsilon c_l x_n}\right\} \tag{19}$$

where:

$$\phi_{ij2} = -c_2\left(P_{ij} - \frac{2}{3}P_k\delta_{ij}\right) \tag{20}$$

Within the viscous sub-layer the wall reflection terms are damped through the function f_w. Their task within the viscous sub-layer is then performed by $(H_{ij} - H_{kk}\,\delta_{ij}/3)$, where H_{ij} is given by equation (21):

$$H_{ij} = f_H\frac{\nu}{k}\left(\overline{u_i u_l}\frac{\partial\sqrt{k}}{\partial x_l}\,\frac{\partial\sqrt{k}}{\partial x_j} + \overline{u_j u_l}\frac{\partial\sqrt{k}}{\partial x_l}\,\frac{\sqrt{k}}{\partial x_i}\right) \tag{21}$$

The term J_{ij}, given in equation (22), increases the sensitivity of the model to the effects of low mean flow Reynolds number:

$$J_{ij} = f_J k\left(\frac{\partial U_i}{\partial x_j} + \frac{\partial U_j}{\partial x_i}\right) \tag{22}$$

The turbulent heat fluxes are obtained through the generalised gradient diffusion hypothesis, as in equation (23):

$$\overline{u_i t} = -c_T\frac{k}{\varepsilon}\overline{u_i u_j}\frac{\partial T}{\partial x_j} \tag{23}$$

In the fully-turbulent region, ε is obtained from the same equation used in the high-Re $k - \varepsilon$ model, equation (8). In the near-wall region, ε is obtained from the wall distance, as in the Wolfshtein (1969) model, but with:

$$\ell_\varepsilon = 2.55\,Y\,[\,1 - \exp(-0.236\,y^*)\,] \tag{24}$$

The damping functions that appear in equations (16)-(22) depend on the dimensionless wall distance y^* and have the following expressions:

$$f_\varepsilon = \exp\left(-\frac{y^*}{3}\right) \tag{25}$$

$$f_w = [1 - \exp(-0.12y^*)][1 - \exp(-0.03y^*)] \tag{26}$$

$$f_J = 0.06\,\exp\left(-\frac{y^*}{3}\right) \tag{27}$$

$$f_H = (10.2 + 7.5y^*) \exp\left(-\frac{y^*}{20}\right) \quad (28)$$

The other modeling constants that appear in the preceding equations have the values given in Table I.

2.3 Problem description and numerical aspects

The flow geometry investigated and the corresponding solution domain is shown in Figure 1. The ribs are placed along the leading and trailing walls, in a staggered arrangement and at an angle of 45° to the main flow direction. The rib spacing to duct height ratio (P/H) is 1, the rib height to duct height ratio (h/H) is 0.1 and the ribs are of square cross-section ($h/w = 1$). For this configuration, flow field data have been measured by Iacovides *et al.* (2003) using LDA for a Reynolds number ($Re = U_b H/\nu$) of 100,000 and for rotation numbers ($Ro = \Omega H/U_b$) of 0 (stationary) and 0.1 (rotating), whilst heat transfer data have collected by Iacovides *et al.* (2001) using liquid crystal for a Reynolds number of 36,000, a Prandtl number of 5.9 (water) and rotation numbers of 0 and 0.2.

The calculations presented here have been carried out using the STREAM code, which employs general non-orthogonal coordinates, with a Cartesian velocity decomposition. A bounded version of the upstream quadratic interpolation scheme, QUICK, described elsewhere (Iacovides, 1999), was employed for the discretization of convection in all transport equations.

A single rib interval was resolved using a body-fitted mesh, which, as can be seen in Figure 2, allows a more efficient resolution of the near-wall regions. The mesh consisted of 74 × 62 nodes within the plane shown in Figure 2 and 60 planes along the direction of the inclined ribs. Periodic flow boundary conditions were imposed. The y^* value of the near-wall nodes was kept, in all computations, to levels of about 1 (in terms of y^+ the value would be about a factor of two lower). As shown by Iacovides (1998) in an earlier study, flow and heat transfer through passages of similar geometries, but with ribs normal to the flow direction, this grid is sufficiently fine to minimize numerical error. Constant wall heat flux thermal boundary conditions were imposed along the two ribbed walls of the duct and adiabatic conditions along the two smooth walls. The surfaces of each rib, in order to be consistent with the experimental conditions, were maintained at a constant temperature. The temperature of each rib was then determined by requiring that the total heat flux from the three surfaces of each rib exposed to the cooling fluid is the same as the total heat flux that crosses from the heated wall into the rib. Further, details can be found in Iacovides (1998), Iacovides and Raisee (1999) and Raisee (1999).

3. Results and discussion

In order to identify the effects of rotation and also in order to present a more extensive evaluation of the capabilities of the turbulence models employed, we start by reviewing

Table I. Turbulence modeling constants

c_μ	σ_k	σ_ε	$c_{\varepsilon 2}$	$c_{\varepsilon 1}$	c_1	c_2	c_1^W	c_2^W	c_T	σ_T
0.09	1	1.22	1.44	1.92	1.8	0.6	0.5	0.3	0.32	0.9

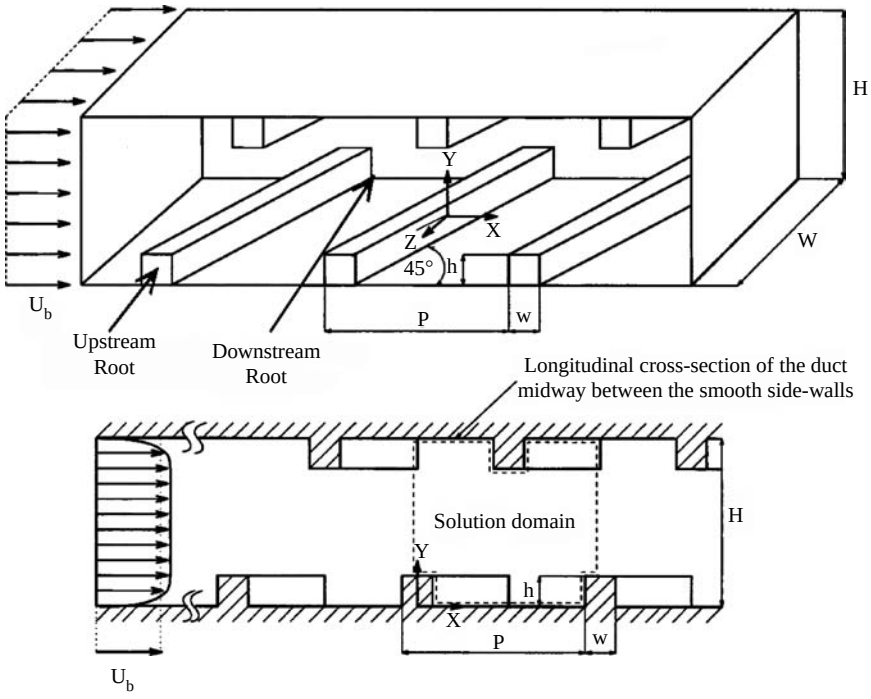

Notes: $P/h = 10$; $h/H = 0.1$ and $h/w = 1$

Figure 1.
Flow geometry

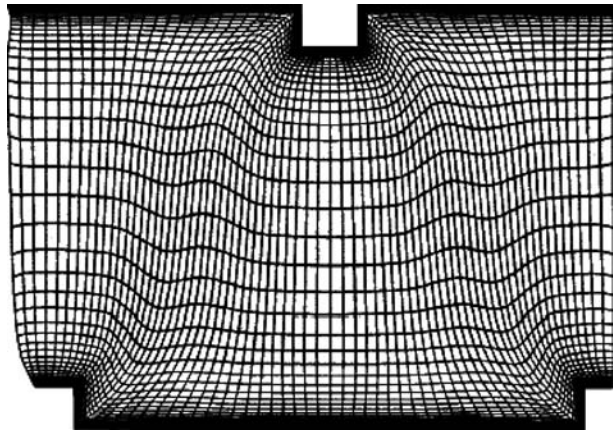

Figure 2.
Body-fitted grid

some of our earlier results, related to the water flow through a heated stationary passage.

Computed vector plots of the motion within cross-duct planes parallel to the inclined ribs, shown in Figure 3(a), reveal that the inclined ribs induce a secondary motion parallel to them. Fluid is transferred along the ribbed walls from the smooth side of the

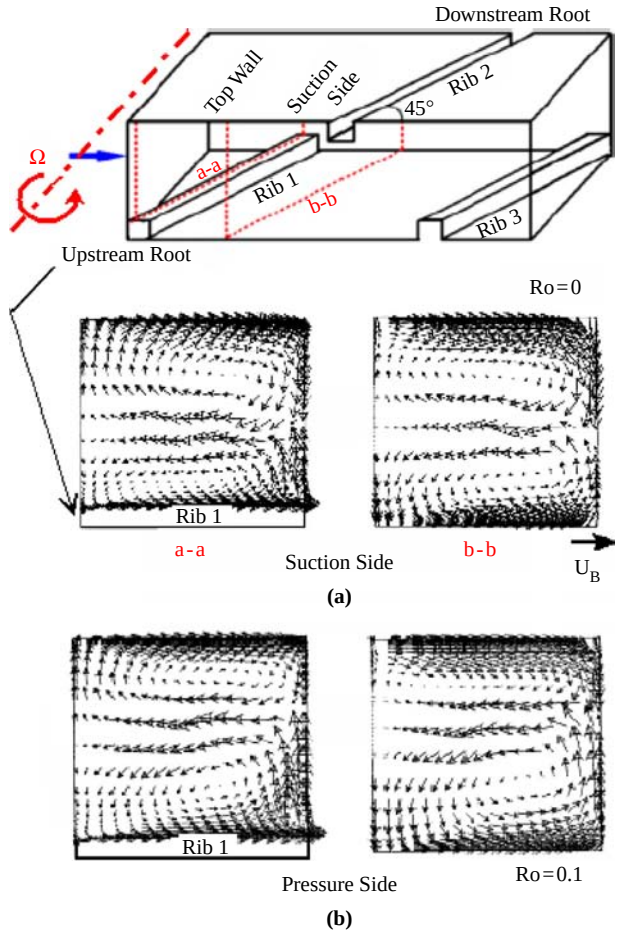

Figure 3.
Predicted secondary motion at $Re = 100{,}000$: (a) stationary case; (b) rotating case

duct that contains the upstream roots, which hereafter will be denoted as the upstream smooth side, of the inclined ribs (the near side in Figure 3) to that containing the downstream rib roots (the far side in Figure 3), which hereafter will be denoted as the downstream smooth side. The cooling fluid is then returned to the upstream smooth side through the center of the duct. One would thus expect the slow moving fluid to be convected to the downstream smooth side and the faster fluid to be displaced towards the opposite smooth (upstream) side.

The computed vector plots of the streamwise motion under stationary conditions, Figure 4(a), confirm this and also show that a consequence of this rib-induced motion is that along the upstream smooth side (near side in Figure 4), section a-a, there is an intense separation bubble after each rib, followed by re-attachment and strong flow acceleration. Along the opposite smooth side, section d-d, the reverse flow after each rib is weak and after re-attachment the streamwise velocity remains low.

Comparisons between the computed and measured axial and cross-duct velocity components along the mid-way plane are shown in Figure 5. They reveal that both

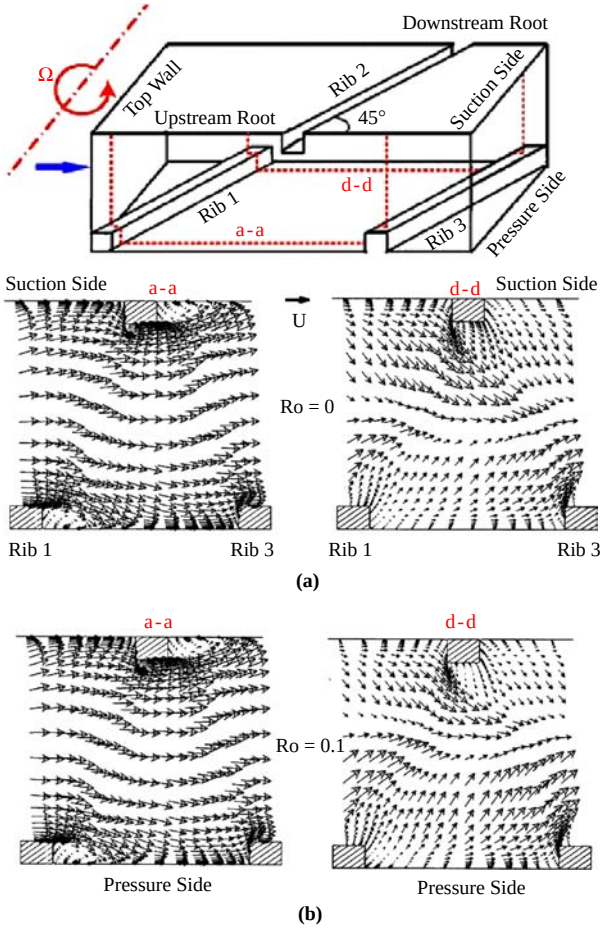

Figure 4.
Predicted streamwise motion at $Re = 100{,}000$: (a) stationary case; (b) rotating case

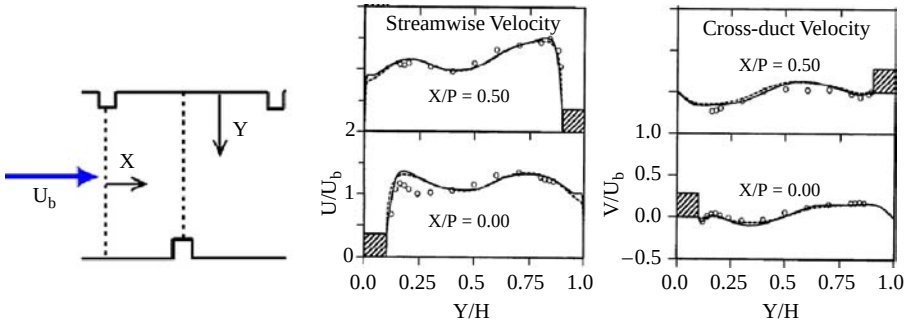

Figure 5.
Comparison between computed and measured mean velocity profiles along the duct mid-plane for stationary case

Notes: Re = 100,000, X and Y as in Figure 1. O Exp., ____ : two-layer DSM; ----- : two-layer $k - \varepsilon$

components of the mean velocity are well reproduced by the two two-layer models employed in this study. This is consistent with the findings of our earlier studies (Iacovides, 1998) of flows through ducts with ribs normal to the flow direction and increases confidence in the conclusions reached from the discussion of Figures 3 and 4. There is practically no difference between the predictions of the two models at the two monitoring locations in Figure 5.

Similar comparisons for the turbulence field, under stationary conditions, are shown in Figure 6. The experimental data show that the levels of turbulence intensity are considerably higher than those found in smooth ducts, but similar to those that we previously measured in straight ducts with normal ribs (Iacovides *et al.*, 2000). Above the surface of each rib, the data show that while both the measured components of the turbulence intensity rise, the streamwise component is significantly higher and also higher than what was previously measured in ducts with normal ribs. Another difference with the measured turbulence field in ducts with normal ribs is that in the case of the 45°-ribs turbulence intensities at the duct center are higher. This must be a consequence of the stronger mixing caused by the rib-induced secondary motion. The profiles of the measured shear stress show that the highest levels occur close to the rib surface and that the shear stress changes sign three times across the duct. Both computations reproduce the overall levels of turbulence intensity but, fail to predict the very high levels of streamwise turbulence intensity measured over the top surface of the ribs. The differences in the intensity predictions of the two models are rather small, especially for the streamwise component. The two-layer $k - \varepsilon$ model generally under-predicts shear stress levels especially at the duct center. The two-layer DSM fails to return the correct sign of the turbulent shear stress at the duct centre, but does produce the correct shear stress distribution over the top of the ribs.

Local Nusselt number comparisons are shown in Figure 7. The experimental contours are shown over two consecutive intervals, in order to show the degree of periodicity present in the data. The measured contours along the ribbed wall, show significant spatial variations in both the streamwise and the spanwise directions. Behind (downstream of) each rib and at the corner with the upstream smooth side, the Nusselt number levels are highest. From there, the *Nu* levels reduce along both the axial and spanwise directions. Along the axial direction, *Nu* levels remain high up to

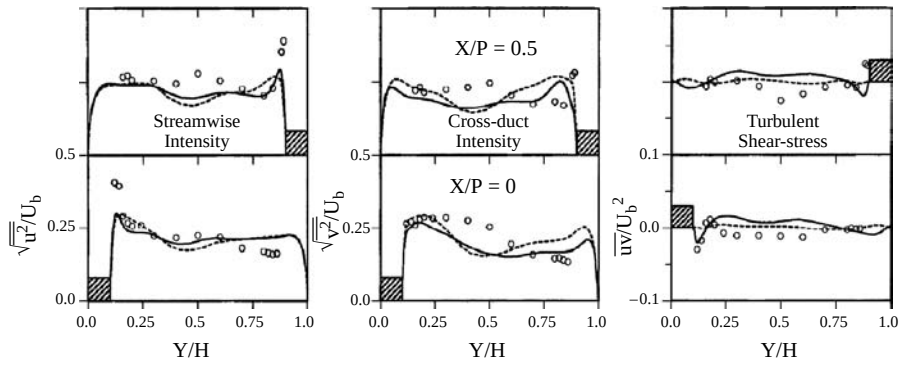

Figure 6.
Comparison between computed and measured turbulent stresses along the duct mid-plane for stationary case

Notes: *Re* = 100,000, *X* and *Y* as in Figure 1. O Exp., ____ : two-layer DSM; ----- : two-layer $k - \varepsilon$

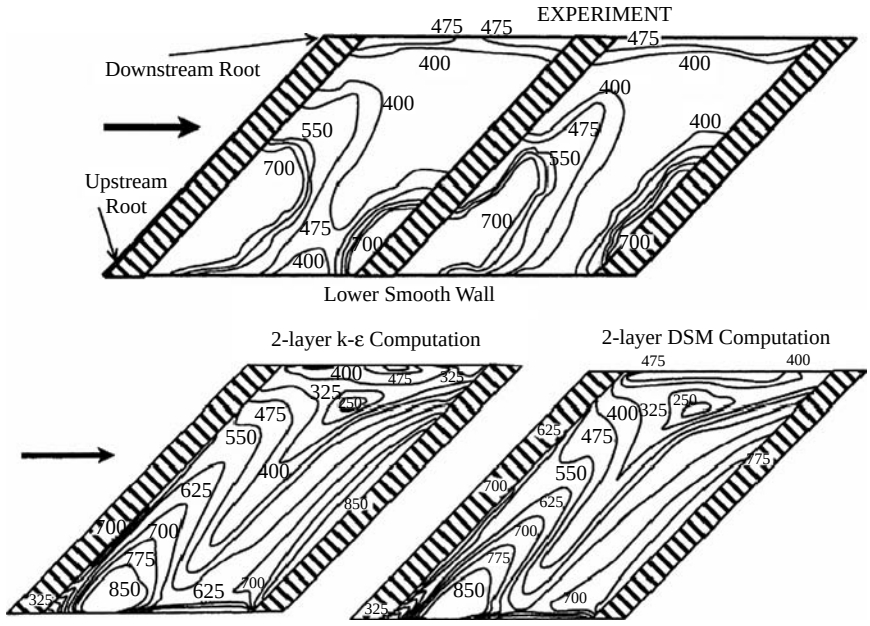

Notes: *Re* = 36,000 and Pr = 5.9 (water)

Figure 7.
Local Nusselt number comparison for stationary case

the mid-way point, while over the second half of the rib interval the Nusselt number falls to a minimum level and then rises again just before the downstream rib. Nusselt number levels also fall, though more gradually, along the spanwise direction, with higher levels along the corner with the upstream smooth side and lower along the corner with the downstream smooth side. This distribution of the local Nusselt number is consistent with the mean flow development. A comparison between Figures 4 and 7 in particular, shows that the high Nusselt number levels close to the upstream smooth wall are caused by the faster moving fluid and intense separation bubble in this region (plane a-a in Figure 4), while the low Nusselt levels close to the opposite smooth wall are caused by the reduction in the streamwise velocity of the fluid and the weak separation bubble (section d-d in Figure 4). The spanwise variation in Nusselt number is thus caused by the spanwise variation in streamwise velocity, which in turn is caused by the rib-induced secondary motion. The two-layer $k - \varepsilon$ computations reproduce the overall Nusselt number variation, though the actual levels measured are somewhat over-predicted. Most notable is the fact that the predicted high Nusselt number region just before the downstream rib, is considerably longer in the spanwise direction, than that measured. The Nusselt number distribution returned by the two-layer DSM is similar to that of the two-layer $k - \varepsilon$. Differences between the local Nusselt number predictions of the two models are mainly confined to the regions just after the upstream rib and just before the downstream rib, where, in closer accord with the measurements, the DSM model produces lower Nusselt number levels than the $k - \varepsilon$ model.

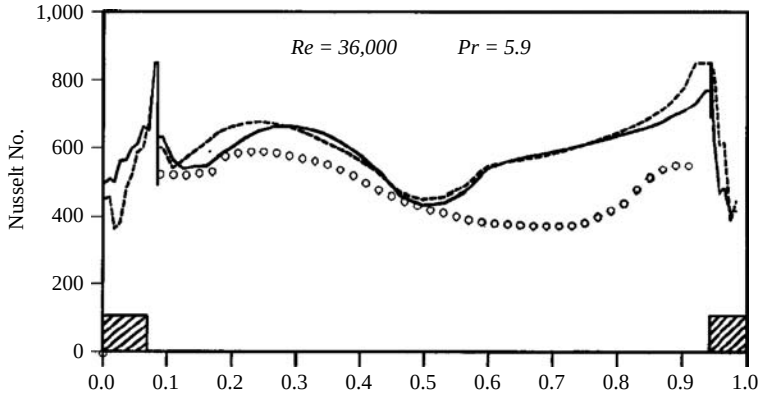

Notes: O Exp., ____ : two-layer DSM; ----- : two-layer $k - \varepsilon$

Figure 8.
Side-averaged Nusselt number comparisons for stationary case (water)

Figure 8 shows a comparison between the measured and computed distributions of side-averaged Nusselt number over the rib interval. The measured distribution shows high levels over the first half of the rib interval gently falling to a minimum level at about three quarters of the way along and then again increasing just before the downstream rib. The computations are in closer agreement with the data over the first half of the rib interval, especially those of the two-layer DSM, though the actual levels are still over-predicted. Over the second half of the rib interval, the side-averaged Nusselt number levels are more strongly over-predicted, especially with the two-layer $k - \varepsilon$, as also observed in the local Nusselt number comparisons. With normal ribs, the two-layer models severely under-predicted the Nusselt number and the differences between thermal predictions of the two-layer $k - \varepsilon$ and DSM models were stronger. It would thus appear that in passages with inclined ribs, the secondary motion makes the modeling of turbulence a less critical, though still important, factor in the prediction of the correct wall heat transfer.

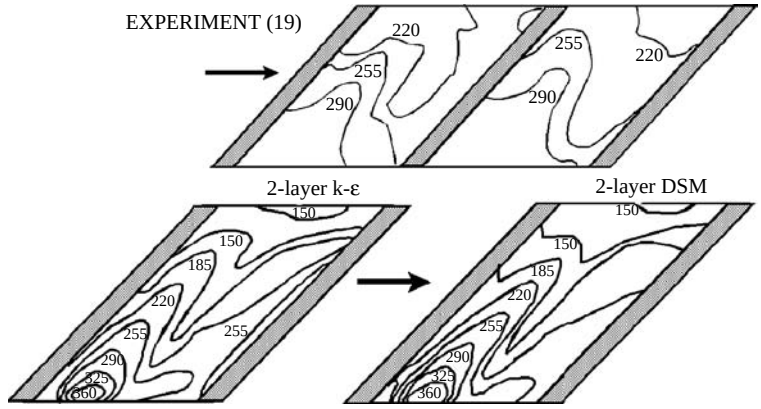

Notes: *Re* = 36,000 and Pr = 0.71(air)

Figure 9.
Local Nusselt number comparison for stationary case

The Nusselt number contours of Figure 9, which are for the same geometry but with air as the cooling fluid, illustrate how the Prandtl number affects the thermal behavior, under stationary conditions and also whether these effects can be reproduced by the numerical simulations. A reduction in the Prandtl number increases the thickness of the sub-layer of the near-wall fluid across which heat conduction, rather than turbulence mixing, is the predominant mode of heat transfer. Therefore, with air as the cooling fluid the influence of near-wall turbulence on wall heat transfer should be weaker than for water. As well as the expected changes in the actual Nusselt number levels, the experimental data for air, like those for water, show the highest Nusselt number levels are encountered after each rib, close to the upstream smooth side and also that from there, the Nusselt number levels fall along both the streamwise and the spanwise directions. In contrast to the water data, the changes in Nu are more gradual along both directions, which is certainly in accord with the effect of the Prandtl number on the thickness of the conduction sub-layer. Both models reproduce the same overall levels as well as a similar distribution. The main difference between the predictions of the two models is that in contrast to the data, the two-layer $k - \varepsilon$ predictions show a modest rise in Nusselt number just before the downstream rib. These comparisons show that, for these cooling passages, use of water results in thermal characteristics similar to those produced by the use of air and also that turbulence models predict the thermal behavior at both Prandtl numbers with similar effectiveness.

Coming now to the effects of rotation, Figure 3(b) shows that the Coriolis force tends to increase the size and strength of the rib-induced vortex along the pressure side, at the expense of the rib-induced vortex along the suction side. This effect is more pronounced along the downstream smooth side. As a result, a comparisons between the vector plots along cut d-d in Figure 4(a) and (b) shows that along the downstream smooth side the flow becomes faster along the pressure side, and the separation bubble after the rib more intense, while along the suction side the flow becomes slower. One would consequently expect that along the pressure side the Nusselt number would fall more gradually along the spanwise direction, from the upstream smooth side to the opposite smooth side, and then this trend to be reversed along the suction side.

As with the stationary case, the validity of the flow predictions is assessed through comparisons between predictions with available measured data, this time along three traverse lines from the pressure to the suction side, all at the same axial location. As in all previous profile comparisons, predicted values at adjacent nodes were interpolated to produce profiles along the traverse experimental lines. The mean flow comparisons, shown in Figure 10, again show that the two sets of predictions are practically identical and in close agreement with the experimental data. Near the upstream smooth side ($Z/H = 0.06$) and also along the mid-plane ($Z/H = 0.5$), the simulations correctly return a rather uniform streamwise velocity. Near the downstream smooth side ($Z/H = 0.94$), the predicted streamwise velocity is high near the pressure side and low near the suction side. The cross-duct velocity near the same smooth side, along both the pressure and suction sides, is directed towards the middle and is stronger near the pressure side. All these predicted features are in agreement with the measurements.

The profiles of turbulence intensities and the turbulent shear stress are shown in Figure 11. Along the mid-plane ($Z/H = 0.5$) the measured turbulence field is similar to that for the stationary case (Figure 6, $X/P = 0.5$). Along the upstream smooth side ($Z/H = 0.06$), turbulence levels are lower, while along the opposite smooth

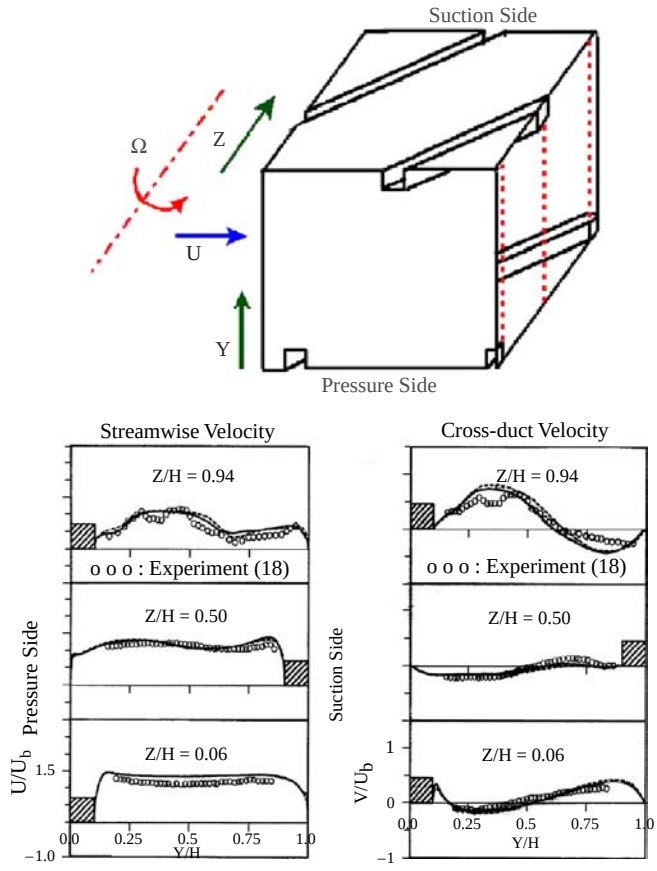

Figure 10.
Mean velocity comparisons for rotating case

Notes: Re =100,000 and Ro = 0.1; ____ : two-layer DSM; ----- : two-layer $k-\varepsilon$

side ($Z/H = 0.94$), turbulence levels are higher than along the mid-plane. This change in the levels of turbulence appears to be consistent with the variation in the strength of secondary velocity shown in Figure 3. As in the stationary case, there are only minor differences between the two sets of predictions which are in close accord with the data. The stronger discrepancies between predictions and measurements are near the downstream smooth side. These comparisons show that the mean flow predictions present an accurate picture of the flow development in a rotating passage with inclined ribs.

The local thermal behavior, under rotating conditions, is presented through the Nusselt number contour plots of Figure 12. The effects of rotation can be deduced through comparisons with the corresponding measured plots for the stationary case (Figure 7). Along the pressure side, the high Nusselt number levels behind the upstream rib and near the upstream smooth side, now extend over a longer distance in the spanwise direction. Over the second half of the rib interval, along the pressure side, there are no substantial differences in the rotating and stationary measured Nu contours. Along the suction side, rotation leads to a more rapid reduction of Nu levels

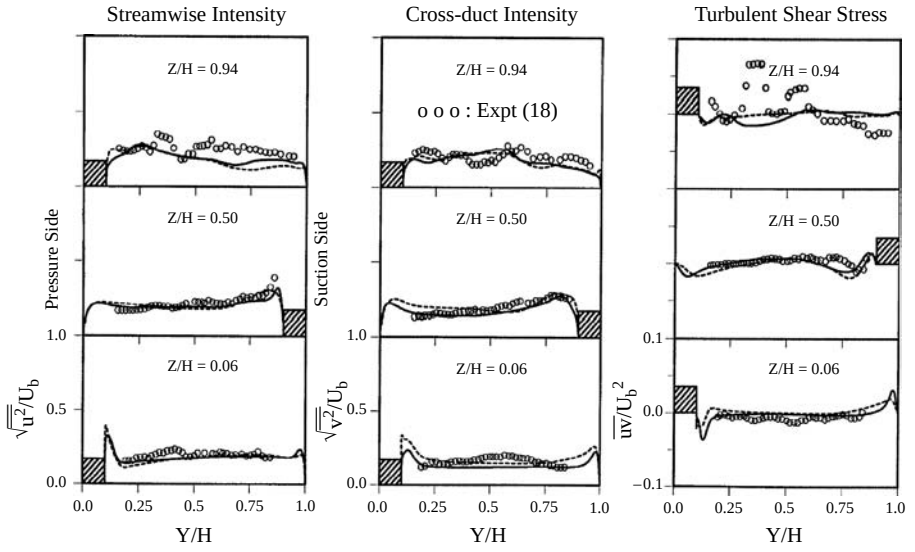

Notes: *Re* =100,000 and *Ro* = 0.1; ____ : two-layer DSM; ----- : two-layer $k - \varepsilon$

Figure 11.
Comparisons of turbulent stresses for rotating case

along the spanwise direction (from the upstream smooth side to the downstream one) both after the upstream rib and before the downstream rib of each interval. These effects of rotation on wall heat transfer along both the pressure and suction sides are consistent with the observed effects of rotation on the mean flow development, discussed earlier. A further feature of rotation along the suction side is the increase in the Nusselt number levels in the corner formed between the downstream rib and the downstream smooth side. The cause of this is not obvious from the flow comparisons. Along the pressure side, both sets of predictions show that after each rib the high *Nu* levels near the upstream smooth side, extend further along the spanwise direction than for the stationary case, a feature consistent with the measurements. Over the second half of the rib interval, both models and especially the effective-viscosity model, as was also the case under stationary conditions, over-predict Nusselt number levels in front of the downstream rib. Along the suction side, both models, and especially the DSM, predict that both after and before each rib the high Nusselt number levels near the upstream smooth side fall more rapidly along the spanwise direction. This is also consistent with the observed effects of rotation on the measured wall heat transfer. Moreover, the DSM predictions also show a small increase in Nusselt number in the corner between the downstream rib and the downstream smooth side.

Finally, the comparisons of the side-averaged Nusselt number of Figure 13, show how effective the computations are in reproducing the overall Nusselt number levels. Along the pressure side, over the upstream half of the rib interval, the measured levels are somewhat higher than for the stationary case, Figure 8, while over the downstream half of the interval they are largely unchanged. While some differences are evident in the measurements for the stationary and rotating cases these are surprisingly small. As already noted in the discussion of Figure 12, the rotation does have a stronger effect on the local Nusselt number contours. The averaging process thus appears to mask the

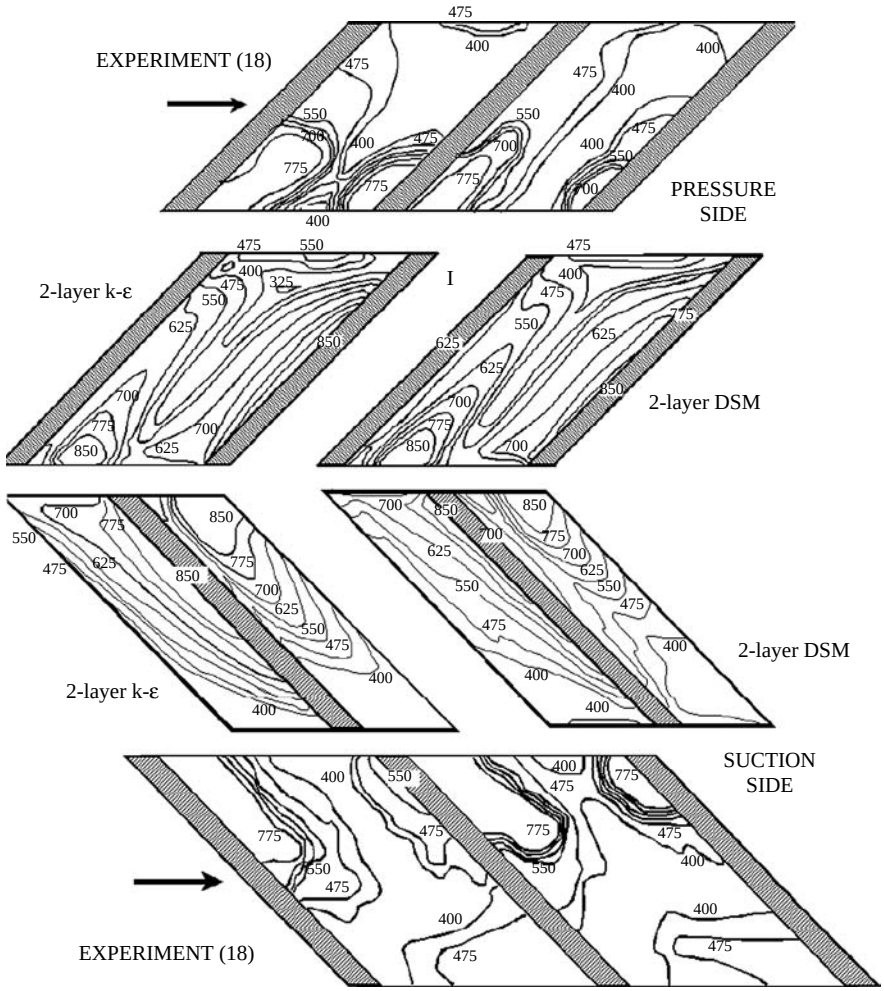

Figure 12.
Local Nusselt number comparison for rotating case

Notes: Re =36,000; Ro = 0.2 and Pr = 5.9

effects of rotation on heat transfer. Both sets of predictions reproduce the correct levels and correct variation over the first half of the interval, while over the second half, as in the stationary case, the measured levels are over-predicted. Along the suction side, over the upstream half of the rib interval, the measured levels are similar to those of the stationary case, while over the downstream half, just before the downstream rib they are somewhat lower. There are now considerable differences between the side-averaged distributions produced by the two models along the suction side, especially over the downstream half. Over the upstream half, the side-averaged levels are well reproduced by both models, with the DSM being rather closer. Over the downstream half, the effective-viscosity model continues to over-predict the side-averaged levels by about as much as along the pressure and stationary sides. The DSM on the other hand, while still

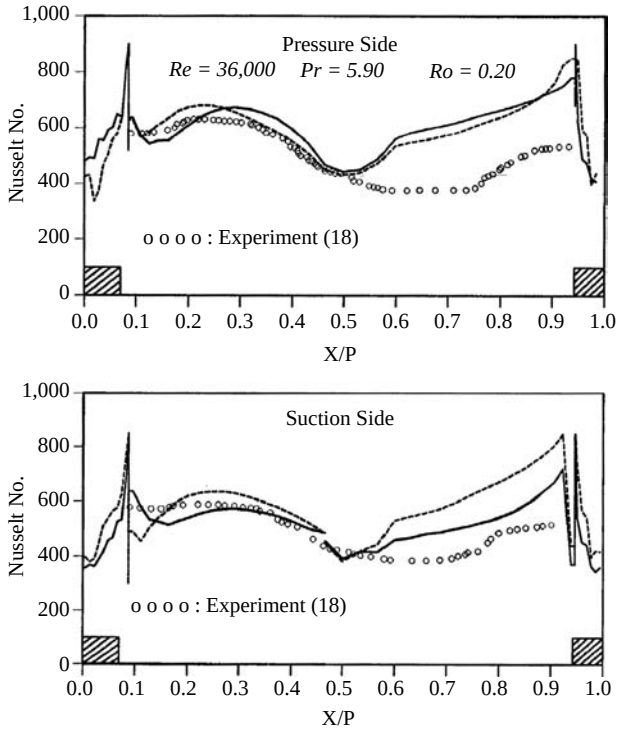

Notes: ____ : two-layer DSM; ----- : two-layer $k - \varepsilon$

Figure 13.
Side-averaged Nusselt number comparisons for rotating case

over-predicting the measured levels, more than halves the difference between the effective-viscosity predictions and the measurements.

In summary, in passages with inclined ribs, for stationary and rotating conditions and also for Prandtl number values ranging from those of air to those of water, both models tested reproduce most of the main features of the local Nusselt number variation, as well as the overall levels, with the second-moment closure offering some additional predictive advantages. The main predictive deficiency is the over-estimation of the Nusselt number levels over the downstream half of the rib interval. The question that arises, is how can the thermal predictions, which as far as blade cooling applications are concerned are the most important part of the numerical simulation, be further improved. It is certainly tempting to reach the conclusion that this is as far as RANS can go and only 3D time-dependent methods can lead to substantial further improvements in the thermal predictions. The fact, however, that under both stationary and rotating conditions, the RANS predictions of the flow field are in very close agreement with measured mean and fluctuating velocity fields, suggests that the main weakness is in the modeling of the near-wall turbulence. A further sensible step might therefore be to explore what further improvements can be achieved through the introduction of low-Reynolds-number models, at EVM (linear and nonlinear) and DSM levels. The authors' earlier experimental investigations (Iacovides *et al.*, 2003, 2001), did show that some large-scale fluctuations are also present. This suggests that the

more expensive 3D and time-dependent approaches such as unsteady RANS or large eddy simulation, may be necessary. The present set of heat and fluid flow comparisons establishes a base-level against which similarly comprehensive comparisons that involve more advanced approaches can be assessed.

4. Concluding remarks

The computations have shown first how the rib-induced secondary motion influences the mean and turbulent flow fields and also the wall heat transfer in flows through ducts with 45° ribs and then how this behavior is further modified by orthogonal rotation. The rib-induced secondary motion creates strong spanwise variation in the mean flow. High-momentum fluid is transported, through the duct core, towards the smooth wall adjacent to the upstream roots of the inclined ribs and the low-momentum fluid accumulates along the opposite smooth wall adjacent to the downstream rib roots. As a result, behind each rib the separation bubble is intense near the upstream root, with the intensity falling towards the downstream root. Moreover, the secondary motion leads to a uniform distribution of the turbulence intensities across the duct. Another consequence of the rib-induced secondary motion is the large spanwise variation in the local Nusselt number along the ribbed walls, with the higher levels encountered along the corner with the smooth wall that contains the upstream rib roots. A reduction in the Prandtl number from that of water to that of air, while leading to more gradual variations in the local wall heat transfer does not change the main thermal characteristics. Orthogonal rotation strengthens the rib-induced vortex that is on the pressure side of the rotating passage. This in turn increases the streamwise velocity of the cooling fluid along the duct pressure side with the reverse effect along the suction side. Consequently, along the pressure side, the high Nusselt number levels encountered after each rib at the vicinity of the smooth upstream wall, fall more gradually in the spanwise direction, while along the suction side, high Nusselt number levels after and before each rib, near the smooth upstream side, fall more rapidly in the spanwise direction.

The two two-layer models of turbulence tested are found to produce satisfactory mean flow predictions and reasonable levels of turbulence intensities, which is consistent with what was found in our earlier studies of flow and heat transfer through ducts with normal ribs. The local and the side-averaged Nusselt number distributions returned by both models include the main features present in the measurements, but over the downstream half of the rib interval actual levels are over-predicted. The two-layer DSM returns lower Nusselt number levels on either side of each rib than the two-layer $k - \varepsilon$, bringing the DSM predictions to closer accord with the measured behavior. This is especially apparent over the downstream half of the rib intervals, along the suction side of the cooling passage, in the case of rotation. The over-prediction of wall heat transfer and also the relatively minor differences in the thermal predictions of the two two-layer models are in contrast to the findings of our earlier numerical studies for passages with ribs normal to the flow direction. The latter suggests that the strong influence of the rib- and Coriolis-induced secondary motion weakens the influence of turbulence on the flow and thermal development.

Further, improvements to the thermal predictions are, nevertheless needed. The comparisons presented here suggest that the next logical step should be to upgrade the model of near-wall turbulence. Flow instabilities observed in experimental studies, on

the other hand point towards the introduction of either unsteady RANS or large eddy simulation.

References

Al-Qahtani, M., Chen, H-C. and Han, J-C. (2002a), "A numerical study of flow and heat transfer in rotating rectangular channels (AR = 4) with 45° rib turbulators by Reynolds stress turbulence model", *Proceedings of ASME Turbo Expo 2002, Amsterdam, The Netherlands*, Paper GT-2002-30216.

Al-Qahtani, M., Jang, Y-J., Chen, H-C. and Han, J-C. (2002b), "Prediction of flow and heat transfer in rotating two-pass rectangular channels with 45-deg rib turbulators", *ASME Journal of Turbomachinery*, Vol. 124, pp. 242-50.

Bonhoff, B., Tomm, U., Johnson, B.V. and Jennions, I. (1997), "Heat transfer predictions for rotating U-shaped coolant channels with skewed ribs and with smooth walls", ASME Paper 97-GT-162, paper presented at International Gas-Turbine and Aero Congress, Orlando, FL.

Bonhoff, B., Parneix, S., Leusch, J., Johnson, B.V., Schabacker, J. and Bölcs, A. (1999), "Experimental and numerical study of developed flow and heat transfer in coolant channels with 45 degree ribs", *International Journal of Heat and Fluid Flow*, Vol. 20, pp. 311-9.

Garcia, G.S. (1998), "An improved liquid-crystal technique for the investigation of convective heat transfer in a square-ended bend", MSc dissertation, Department of Mechanical Engineering, UMIST, Manchester.

Gibson, M.M. and Launder, B.E. (1978), "Ground effects on pressure fluctuations in atmospheric boundary layers", *Journal of Fluid Mechanics*, Vol. 86, pp. 491-551.

Han, J.C. and Zhang, Y.M. (1991), "Effect of rib-angle orientation on local mass transfer distribution in a three-pass rib-roughened channel", *ASME Journal of Turbomachinery*, Vol. 113, pp. 123-30.

Han, J.C., Glicksman, L.R. and Rosenhow, W.M. (1988), "An investigation of heat transfer and friction of rib-roughened surfaces", *International Journal of Heat and Mass Transfer*, Vol. 31 No. 1, pp. 183-95.

Iacovides, H. (1998), "Computation of flow and heat transfer through rotating ribbed passages", *International Journal of Heat and Fluid Flow*, Vol. 19, pp. 393-400.

Iacovides, H. (1999), "The computation of turbulent flow through stationary and rotating U-bends of with rib-roughened surfaces", *International Journal on Numerical Methods in Fluids*, Vol. 29, pp. 865-76.

Iacovides, H. and Launder, B.E. (1992), "The computation of convective heat transfer in a 180° pipe bend", paper presented at ICHMT, International Symposium on Heat Transfer in Turbomachinery, Athens.

Iacovides, H. and Launder, B.E. (1995), "Computational fluid dynamics applied to internal cooling of gas-turbine blade cooling: a review", *International Journal of Heat and Fluid Flow*, Vol. 16, pp. 454-70, Review Article.

Iacovides, H. and Raisee, M. (1999), "Recent progress in the computation of flow and heat transfer in internal cooling passages of turbine blades", *International Journal of Heat and Fluid Flow*, Vol. 20, pp. 320-8.

Iacovides, H. and Toumpanakis, P. (1993), "Turbulence modelling of flow in axisymmetric rotor-stator systems", *Proceedings of IAHR, 5th International Symposium on Refined flow modelling and Turbulence Measurements, Paris*.

Iacovides, H., Kelemenis, G. and Raisee, M. (2003), "Flow and heat transfer in straight cooling passages with inclined ribs on opposite walls: an experimental and computational study", *Journal of Experimental Thermal Fluid Science*, Vol. 27, pp. 283-95.

Iacovides, H., Jackson, D.C., Kelemenis, G. and Launder, B.E. (2000), "The measurement of local wall heat transfer in stationary U-ducts of strong curvature, with smooth and rib-roughened walls", *ASME Journal of Turbomachinery*, Vol. 122, pp. 386-92.

Iacovides, H., Jackson, D.C., Kelemenis, G., Launder, B.E. and Yuan, Y-M. (2001), "Dynamic and thermal measurements of flow in a rotating U-bend with 45° ribs", *International Journal of Heat and Fluid Flow*, Vol. 22, pp. 308-14.

Iacovides, H., Jackson, D.C., Ji, H., Kelemenis, G., Launder, B.E. and Nikas, K-S. (1998), "LDA study of flow development through an orthogonally rotating U-bend of strong curvature and rib-roughened walls", *ASME Journal of Turbomachinery*, Vol. 108, pp. 386-91.

Jang, Y-J., Chen, H-C. and Han, J-C. (2001), "Flow and heat transfer in a rotating square channel with 45 deg angled ribs by Reynolds stress turbulence model", *ASME Journal of Turbomachinery*, Vol. 123, pp. 124-32.

Johnson, B.V., Wagner, J.H., Steuber, G.D. and Yah, F.C. (1994), "Heat transfer in rotating serpentine passage with trips skewed to the flow", *ASME Journal of Turbomchinery*, Vol. 116, pp. 113-23.

Lin, Y-L., Shih, T.I-P., Stephens, M.A. and Chyu, M.K. (2001), "A numerical study of flow and heat transfer in a smooth and ribbed U-duct with and without rotation", *ASME Journal of Heat Transfer*, Vol. 123, pp. 219-32.

Liou, T-M. and Dai, G-Y. (2003), "Pressure and flow characteristics in a rotating two-pass square duct with 45-deg angled ribs", ASME Paper, 2003-GT-38346, paper presented at International Gas-Turbine and Aero Congress, Atlanta, GA.

Raisee, M. (1999), "Computation of flow and heat transfer through two- and three-dimensional ribbed passages", PhD thesis, Department of Mechanical Engineering, UMIST, Manchester.

Taslim, M.E., Li, T. and Kercher, D.M. (1996), "Experimental heat transfer and friction in channels roughened with angled, V-shaped and discrete ribs on two opposite walls", *ASME Journal of Turbomachinery*, Vol. 118, pp. 20-8.

Wolfshtein, M. (1969), "The velocity and temperature distribution in one-dimensional flow with turbulence augmentation and pressure gradient", *International Journal of Heat and Mass Transfer*, Vol. 12, pp. 301-18.

Corresponding author
Mehrdad Raisee can be contacted at: mraisee@ut.ac.ir